Nanoscale Advances

ROYAL SOCIETY OF CHEMISTRY

PAPER

View Article Online
View Journal | View Issue

Cite this: *Nanoscale Adv.*, 2026, **8**, 859

Strategic tuning of precursor's concentration for the synthesis of Sb_2S_3 thin films with enlarged nanocrystals and *hk*1-oriented growth, leading to superior optical properties

Md Abrar Faisal Hossain, *[a] Kyota Shirai[b] and Masayuki Shimojo †[b]

Antimony trisulfide (Sb_2S_3) has acquired significant attention due to its non-toxic nature, durability, abundance, and superior opto-electronic properties, making it a promising candidate for various applications in optoelectronics and photovoltaics. It is important to focus on achieving the desired crystal morphology and preferred growth (*hk*1-oriented), as these can potentially result in superior optical properties. Moreover, surface morphology and stoichiometric ratio of the fabricated films also play a significant role. Even after conducting intensive research to address these factors, there remains immense research scope to enhance these properties. In this study, we present a strategically optimized precursor concentration for solution-based synthesis of Sb_2S_3 thin films with large, compact, homogeneous nanocrystals, *hk*1-oriented preferential growth and superior optical properties, through a simple, cost-effective spin coating method. By varying the concentration of CS_2 (source of sulphur), an enhanced precursor solution was synthesized, which yielded the desirable crystal dimensions, *hk*1-oriented growth and optical properties. In this research work, we demonstrate the results of varying the concentration of CS_2 (from 1.5 ml to 3 ml with steps of 0.5 ml) and the effect it has on the overall structural and optical properties. The synthesized materials were characterized comprehensively using High-Resolution Transmission Electron Microscopy (HR-TEM), Bright-Field Transmission Electron Microscopy (BF-TEM), Selected Area Electron Diffraction (SAED), Scanning Electron Microscopy (SEM), Energy-Dispersive X-ray Spectroscopy (EDS), and Variable Angle Spectroscopic Ellipsometry (VASE). Our experimental findings of BF-TEM, HR-TEM, SAED, and VASE conclude that the precursor solution consisting of 2.5 ml of CS_2 was able to generate enhanced nanocrystals, *hk*1-oriented growth and superior optical properties. The other measurements taken using the characterizing techniques agreed well with the findings of BF-TEM, HR-TEM, SAED, and VASE.

Received 20th September 2025
Accepted 10th November 2025

DOI: 10.1039/d5na00901d

rsc.li/nanoscale-advances

1. Introduction

Metal chalcogenide (MC) semiconductors of type M_2X_3 (where M = As, Sb, Bi; X = S, Se, Te) have particularly gained substantial research interest recently due to their applications in photovoltaics,[1–4] thermoelectrics,[5–7] optoelectronics,[8–11] memory devices,[12,13] photocatalysis[14] and neuromorphic implementation.[15] Among such M_2X_3 semiconductor materials, antimony trisulfide (Sb_2S_3) with a quasi-one-dimensional ribbon like structure has shown significant promise due to its excellent photosensitivity and thermoelectric power,[16] specified quantum size effects,[17] high absorption coefficient ($\sim 10^5$ cm^{-1} over the UV-visible range)[18] and refractive index,[19] optimum optical band gap (around 1.7 eV),[20] along with low toxicity, ample abundancy and great durability. Owing to these properties, antimony trisulfide has found its way into inorganic heterojunction, hybrid and dye-sensitized solar cells.[21–23] Sb_2S_3 has also proven to be a potential material for applications in thermoelectric cooling, optoelectronics, microwave devices and television cameras.[24]

To date, there have been many synthesis and deposition routes suggested by researchers for fabricating Sb_2S_3 thin films, which can roughly be categorized into vacuum-assisted and solution-processed methods. Vacuum-assisted methods may include Rapid Thermal Evaporation (RTE), Vapor Transport Deposition (VTD), Close Space Sublimation (CSS), and magnetron sputtering.[25] Solution-processed methods include Hydrothermal Deposition (HD), spin-coating, and Chemical Bath Deposition (CBD).[18] Solution-processed synthesis methods have achieved considerable interest due to their low cost, ease of

[a]*Department of Mechanical Engineering, The Hong Kong Polytechnic University, 11 Yuk Choi Road, Hung Hom, Hong Kong, China. E-mail: abrar.hossain@connect.polyu.hk; Tel: +852 6683 7589*

[b]*Department of Materials Science and Engineering, Shibaura Institute of Technology, 3-7-5 Toyusu, Koto, Tokyo, 135-8548, Japan*

† Supervising author.

fabrication, rapid production, scope of large-area manufacturing, and most importantly their ability to generate large grain sized films, thereby reducing the grain boundary density and improving the device performance.[26] Among the solution-processed methods, the most prominent deposition technique is regarded to be the spin-coating method, as other methods like CBD result in a greater generation of chemical waste, are time-intensive, and produce high impurity levels, while HD necessitates a more costly experimental setup.[27] Solution-processed methods generally include the development of a precursor solution, which eventually leads to the formation of the thin film. Depending on the precursor formulation, a suitable method of fabricating (CBD, HD, or spin-coating) the thin film is chosen. The precursor solution synthesis route proposed by Wang *et al.*,[28] an easy one-step precursor formulating method which involves dissolving Sb_2O_3 in ethanol-diluted butyldithiocarbamic acid (BDCA), is also applied in this work with deliberate modifications.

Surface defects, unfavourable *hk*0 orientations, and high grain boundary density are the major setbacks commonly faced in fabricating thin films of metal chalcogenides. Thus far, there have been many efforts made to tackle such challenges *via* engineering precursor molar ratios,[27,29,30] introducing additional sulphur sources during performing Chemical Bath Deposition (CBD) and Vertical Transport Deposition (VTD),[31,32] *in situ* addition of Cd^{2+} ions or tartaric acid during Hydrothermal Deposition (HD),[33,34] and performing post-treatment of the film by spin-coating an $SbCl_3$ layer on Sb_2S_3.[35] Such efforts were made to achieve an ideal stoichiometric ratio (Sb : S, 2 : 3), uniform morphology mitigating defects and pinholes, favourable *hk*1 orientation crystal planes, and a large grain size with reduced grain boundary density. However, most of the vacuum-assisted (VTD and CSS) and some solution-processed (CBD and HD) methods do not allow complete control over the film growth and stoichiometric ratio, making it difficult to address the major film fabrication challenges. Thus, there remains opportunity for improvement in potential film fabrication techniques to achieve stable crystal growth, uniform surface morphology, favourable *hk*1-oriented crystal planes, and reduced grain boundary density.

In this research work, we conducted a comprehensive study on the structural, morphological, compositional, and optical aspects of Sb_2S_3 thin films synthesized *via* a strategically tuned concentration precursor solution. We adopted the precursor solution synthesis route proposed by Wang *et al.*[28] with some deliberate tactical modifications to the concentration of one of the reactants to obtain enhanced film characteristics. As mentioned by Chen *et al.*,[18] solution-processed methods generally yield a reduced grain boundary density compared to vacuum-assisted methods like VTD, CSS, and sputtering. By implementing our strategic precursor solution route, we can deposit our thin film *via* a simple, cost-effective spin coating technique. Our recipe for the precursor solution included antimony trioxide (Sb_2O_3) as the antimony source and carbon disulfide (CS_2) as the carbon source, along with ethanol and butylamine. We carefully increased the CS_2 concentration from 1.5 ml to 3 ml with steps of 0.5 ml, keeping other reactants constant. The thin films fabricated were extensively characterized to study various properties of the deposited thin films.

2. Experimental methods

2.1. Chemicals

Antimony trioxide (FUJIFILM, 95%), carbon disulfide (FUJIFILM, 99%), and *n*-butylamine (FUJIFILM) were purchased from FUJIFILM Wako Pure Chemical Corporation and used without further purification.

2.2. Preparation of antimony trisulfide (Sb_2S_3) precursor solution

The Sb_2S_3 precursor solution, which is essentially a metal–acid (metal–BDCA) complex solution, was prepared following the recipe proposed by Wang *et al.*,[28] with some strategic modifications to it. 1 mmol (0.2915 g of Sb_2O_3) of antimony trioxide (Sb_2O_3) was added to each of the four empty 20 ml glass vials, followed by 2 ml ethanol. Afterwards 1.5–3.0 ml CS_2 was added in steps of 0.5 ml to produce four distinct precursor solutions. At last, 1 ml of butylamine was added to each of the four solutions. The solution mixtures were stirred overnight for 24 hours to produce a clear solution. For simplicity, from here on, the films produced by these solutions will be referred to as 1.5-Sb_2S_3, 2.0-Sb_2S_3, 2.5-Sb_2S_3, and 3.0-Sb_2S_3 as appropriate.

2.3. Film fabrication and characterization

The obtained precursor solutions were spin-coated on borosilicate glass substrates (purchased from Matsunami) at 6000 rpm for 30 seconds. Before using the glass substrates, they were thoroughly cleaned using an ultrasonic cleaner, with acetone and ethanol, followed by DI water. Upon spin-coating, all the samples were annealed in a vacuum at 300 °C for 30 minutes to obtain a carbon-free crystallized Sb_2S_3 thin film.

High-Resolution Transmission Electron Microscopy (HR-TEM), Bright-Field Transmission Electron Microscopy (TEM), and Selected Area Electron Diffraction (SAED) were performed to obtain High-Resolution (HR) images, Bright-Field (BF) images, and selected area electron diffraction patterns, respectively, using a TEM JEM 2100 (JEOL). Scanning Electron Microscopy (SEM) was performed using a Hitachi S-4500 to observe the surface morphology. Energy Dispersive Spectroscopy (EDS) coupled with SEM was performed using a W-SEM JSM-IT510LA (JEOL) to obtain the chemical composition. A variable angle spectroscopic ellipsometer (RC2-DI-SUY) was used to obtain the optical properties of the thin film.

3. Results and discussion

The annealed films (1.5-Sb_2S_3, 2.0-Sb_2S_3, 2.5-Sb_2S_3, and 3.0-Sb_2S_3) were characterized thoroughly to study and analyse their properties. The obtained results from the characterization process are demonstrated in this section. All the data achieved conclude that 2.5-Sb_2S_3 obtained superior structural and optical properties.

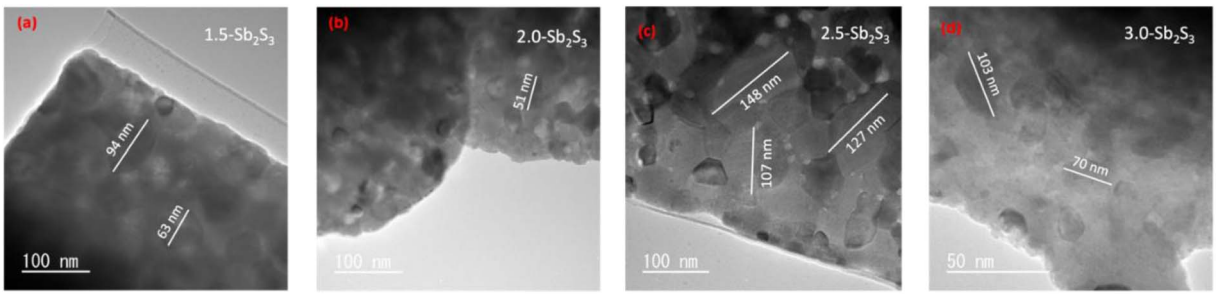

Fig. 1 Bright-field TEM images of the Sb_2S_3 thin films annealed at 300 °C: (a) 1.5-Sb_2S_3, (b) 2.0-Sb_2S_3, (c) 2.5-Sb_2S_3, and (d) 3.0-Sb_2S_3.

3.1. Bright-field TEM and high-resolution TEM

Bright-field TEM and high-resolution TEM images of the 4 samples (1.5-Sb_2S_3, 2.0-Sb_2S_3, 2.5-Sb_2S_3, and 3.0-Sb_2S_3) acquired with a TEM are shown in Fig. 1 and 2, respectively. Solution-processed and spin-coated samples are often difficult to analyse with a TEM due to the complexity associated with transferring the sample to the TEM mesh/grid. In this research, we adopted adhering the TEM mesh on the glass substrate using carbon tape and then performing the spin coating on the mesh/glass substrate. After completion of spin coating, the carbon tape was peeled off, and the mesh was heated in a vacuum for 30 minutes at 300 °C. This TEM sample preparation method ensured that the film was free of any physical contact and provided reliable, accurate results. The bright-field TEM images obtained with an accelerating voltage of 200 kV are shown in Fig. 1, which reveal the nanocrystalline structure of the fabricated thin films. 2.5-Sb_2S_3 (Fig. 1(c)) shows more uniform crystal thickness compared to 1.5-Sb_2S_3 (Fig. 1(a)) and 2.0-Sb_2S_3 (Fig. 1(b)), and 2.5-Sb_2S_3 has much larger crystals (~120 nm) (Fig. 1(c)) than 1.5-Sb_2S_3 (~70 nm) (Fig. 1(a)), 2.0-Sb_2S_3 (~50 nm) (Fig. 1(b)), and 3.0-Sb_2S_3 (~90 nm) (Fig. 1(d)). Incorporating 1.5 ml and 2.0 ml of CS_2 proved to be insufficient to saturate all nucleation sites; as a result, some region remained underdeveloped, leading to local variations in crystal thickness. However, some tiny white particles can be observed along the boundaries, which are likely residual nuclei of Sb_2S_3.[28] Fig. 1(a) and (b) can be observed to have similar morphological properties with non-uniform thickness and smaller crystals.

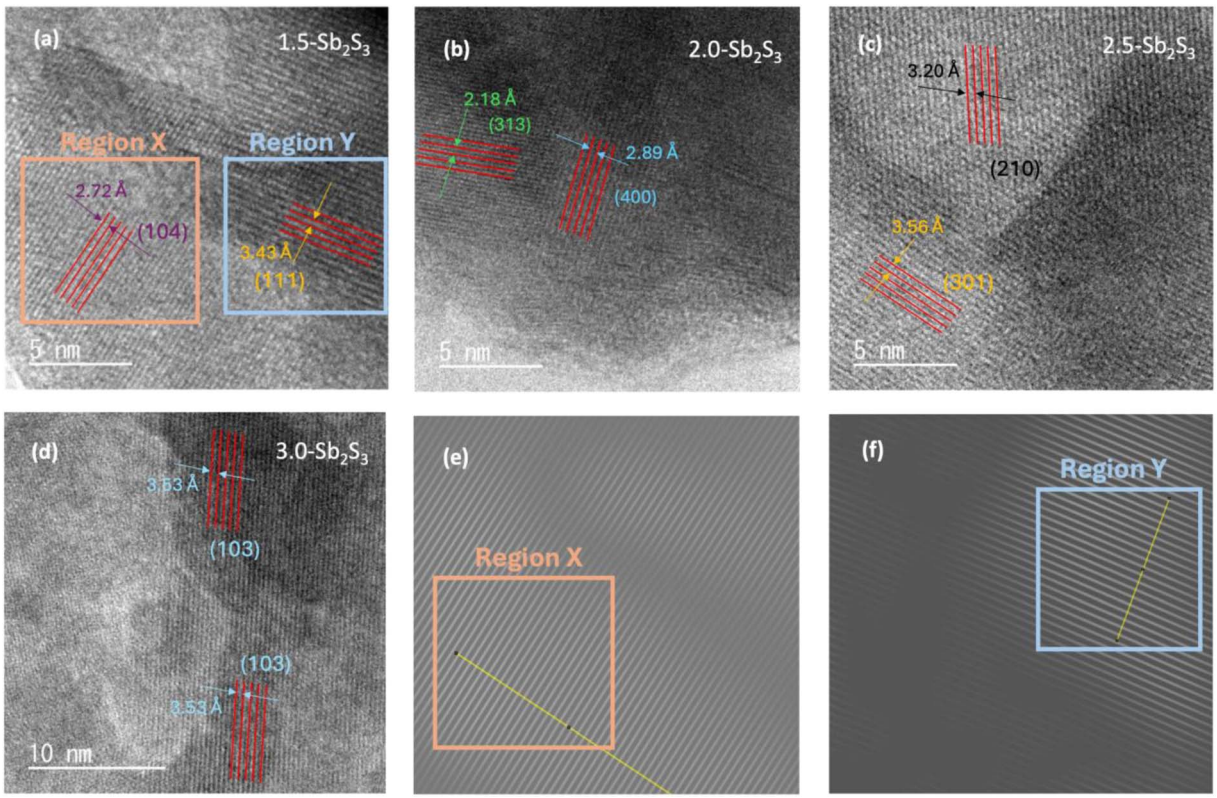

Fig. 2 HR-TEM images of the Sb_2S_3 thin films annealed at 300 °C: (a) 1.5-Sb_2S_3, (b) 2.0-Sb_2S_3, (c) 2.5-Sb_2S_3, and (d) 3.0-Sb_2S_3. FFT-diffractogram images of 1.5-Sb_2S_3 in (e) region X and (f) region Y.

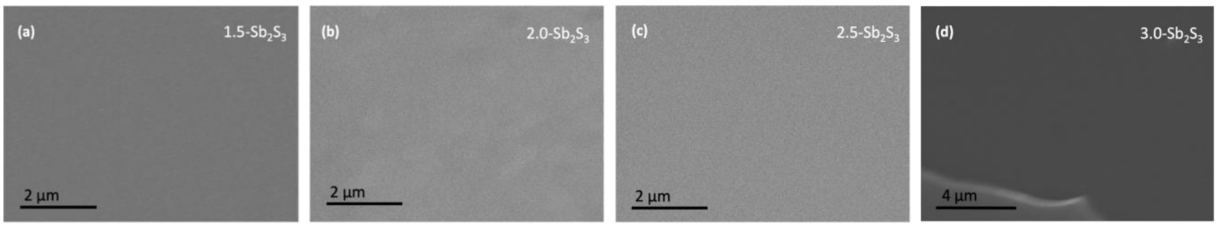

Fig. 3 Top-view SEM images of the Sb_2S_3 thin films annealed at 300 °C: (a) 1.5-Sb_2S_3, (b) 2.0-Sb_2S_3, (c) 2.5-Sb_2S_3 and (d) 3.0-Sb_2S_3.

Therefore, increasing the CS_2 concentration to 2.5 ml yielded larger nanocrystals (nearly twice the size of 1.5-Sb_2S_3 and 2.0-Sb_2S_3) and more uniform crystal thickness.

High-resolution TEM images were taken using a TEM to observe the overall morphology of the crystal lattice as shown in Fig. 2. HR-TEM images of the four samples show visible lattice fringes confirming the crystallinity of the samples. Some differences in uniformity can be observed, which shows the relative overlapping of different lattice fringes. No evident crystal defects such as dislocation of the lattice fringes can be observed from the high-resolution TEM images at a resolution of 5–10 nm. Hence, all the fabricated films possessed well-resolved lattice fringes without any obvious evidence of structural defects. Furthermore, to analyse the crystal plane, Fast Fourier Transform (FFT) was performed on the lattice fringes with the help of ImageJ software. This helped to measure the interplanar spacing (*d*-spacing) of the lattice accurately. FFT-diffractogram images of lattice fringes of 1.5-Sb_2S_3 are shown in Fig. 2(e) (representing region "X") and Fig. 2(f) (representing region "Y"). Measuring the *d*-spacing of these lattice fringes revealed $d = 2.72$ Å (104) for region X and $d = 3.43$ Å (111) for region *Y*. Similarly, FFT diffraction was also performed on other samples. 2.0-Sb_2S_3 showed $d = 2.18$ Å (313) and $d = 2.89$ Å (400), Fig. 2(b). 2.5-Sb_2S_3 fringes (Fig. 2(c)) demonstrated interplanar *d*-spacings of $d = 3.20$ Å (210) and 3.56 Å (301). Lastly, 3.0-Sb_2S_3 showed $d = 3.53$ Å (103). Therefore, high-resolution TEM images confirmed the crystallinity across all the samples with no evident defects (dislocations), whereas bright-field TEM images revealed the large crystal sizes of 2.5-Sb_2S_3.

3.2. Scanning electron microscopy (SEM)

Scanning electron microscopy was performed to understand the surface morphology of the annealed thin films. Fig. 3(a)–(d) show the obtained top-view SEM images of the samples. All the SEM images display a compact, homogeneous surface morphology at the micron scale (around 2 μm). No visible grain boundaries could be seen at such a scale, which disregards the presence of any dense grain boundary region. This shows that the surface is free of any suppressing defect states and ensures efficient charge transport, which is significant for photovoltaic applications. The absence of large and visible cracks and pinholes at such a scale confirms the uniform, compact, spin-coated and annealed films. These findings support the superior surface morphology of the fabricated films, only at the micron scale. It is worth noting that the parameters related to SEM measurements (accelerating voltage, magnification) were adjusted to certain values but did not produce any visible boundaries or defects. Hence, the top-view SEM images of the fabricated thin films show impressively compact and homogeneous surface morphology without the presence of visible dense grain boundaries.

3.3. Selected area electron diffraction (SAED) pattern

The SAED pattern was performed using a TEM to identify the orientation of the crystal planes (Miller indices) across a selected area of nanocrystals and to analyse the corresponding diffraction spots. SAED patterns can reveal crystal planes (rings corresponding to XRD peaks), which cannot be observed in XRD for nanocrystalline films. Fig. 4(a)–(d) show the SAED patterns obtained for 1.5-Sb_2S_3, 2.0-Sb_2S_3, 2.5-Sb_2S_3, and 3.0-Sb_2S_3, respectively. The SAED patterns of all the samples show bright diffraction spots, and the absence of any diffused rings proves that there are no amorphous regions. Hence, all the samples obtained show a pure crystalline phase with no amorphous regions. It is important to note that the observation area used in generating the SAED patterns were constant across all the samples. Hence, when a dense diffraction pattern is obtained, it refers to the existence of many small crystals with different orientations, in the area selected for diffraction. This concept is illustrated in Fig. 4(g), where six differently oriented crystals produce a dense diffraction pattern. In contrast, when a sparse diffraction pattern is obtained, it refers to the existence of lower number of crystals and of bigger size, as the selected area aperture was the same. This is illustrated in Fig. 4(h). Following these concepts, it can be concluded that 2.0-Sb_2S_3 (Fig. 4(b)) and 3.0-Sb_2S_3 (Fig. 4(d)) possessed smaller crystals as the SAED patterns showed some areas of dense diffraction spots. Interestingly, the SAED pattern of 2.5-Sb_2S_3 (Fig. 4(c)) also shows some region of dense diffraction pattern, revealing the presence of smaller crystals. This could be explained by the BF-TEM findings of 2.5-Sb_2S_3, which show bigger (~130 nm) and also smaller (~60 nm) crystals.

The Miller indices (*hkl*) representing the orientation of the crystal planes were calculated using eqn (1) for a polycrystalline orthorhombic structure, where *d* is the interplanar spacing and *a*, *b*, and *c* are the lattice constants with values $a = 11.31$ Å, $b = 3.83$ Å, and $c = 11.23$ Å.

$$\frac{1}{d^2} = \frac{h^2}{a^2} + \frac{k^2}{b^2} + \frac{l^2}{c^2} \quad (1)$$

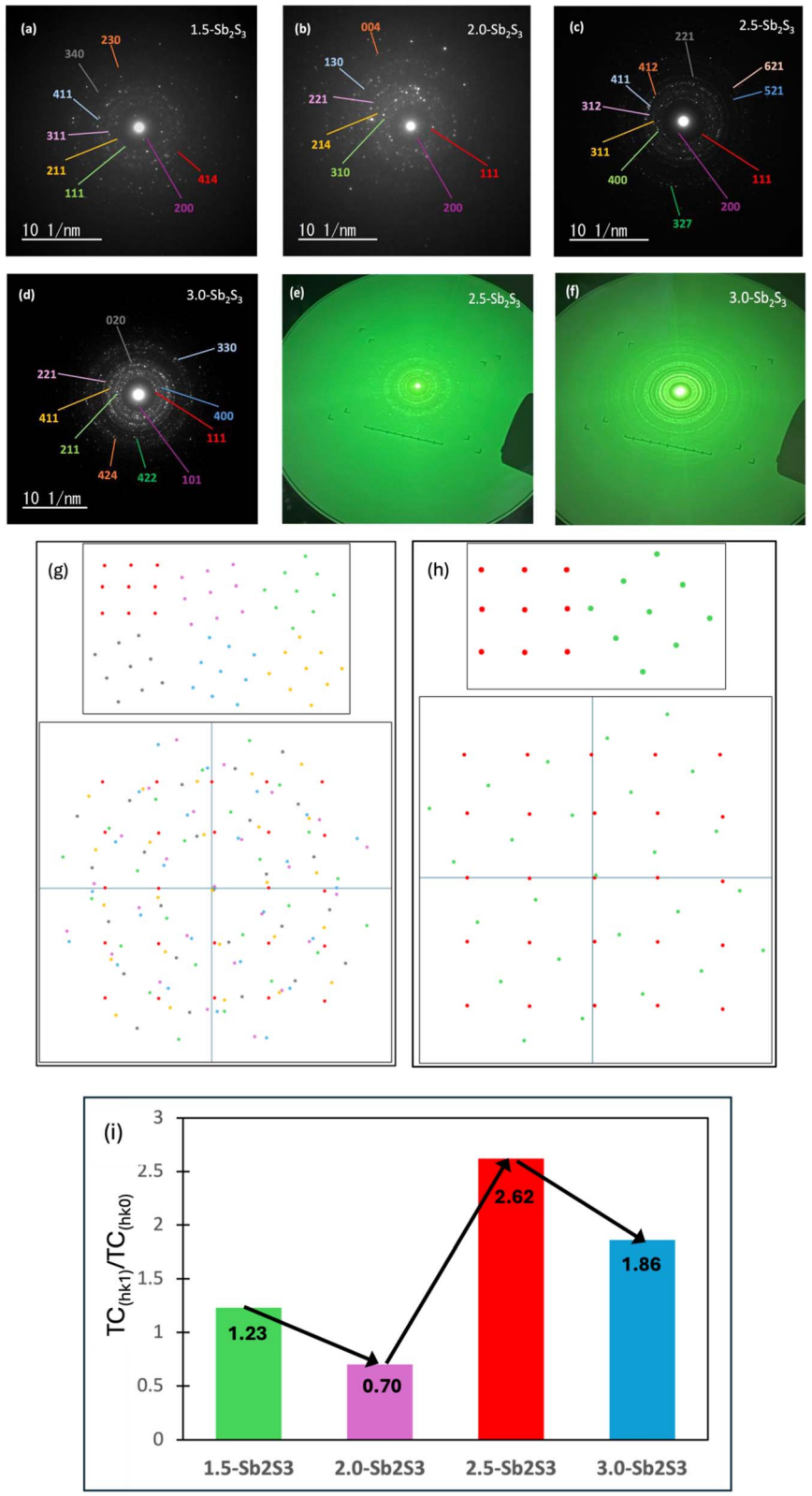

Fig. 4 SAED pattern images of the Sb_2S_3 thin films: (a) 1.5-Sb_2S_3, (b) 2.0-Sb_2S_3, (c) 2.5-Sb_2S_3 and (d) 3.0-Sb_2S_3. Electron diffraction images of (e) 2.5-Sb_2S_3 and (f) 3.0-Sb_2S_3, captured with an external camera. Illustration of diffraction patterns of dense (g) and sparse (h) regions. (i) Texture coefficients ($TC_{(hk1)}/TC_{(hk0)}$).

The value of interplanar spacing (d) was calculated by measuring the diameter (D) of the ring, followed by the radius ($r = D/2$), and then taking the reciprocal of the radius ($1/r$). All the units were converted to Ångström (Å) before starting the calculation. Different values of h, k, and l (in ascending order) were fit to eqn (1), and the values that generated the least error were selected. When looking at the Miller indices, it could be seen that the samples have preferential growth in the $hk1$ direction proven by the texture coefficients (TC) ($hk1/hk0$) shown in Fig. 4(g), which is beneficial for optoelectronic devices to achieve high efficiency.[18] It is worth noting that solution-processed spin-coated samples usually tend to favour $hk0$-oriented growth of the Sb_4S_6 nanoribbons; however, in our research work, we have successfully demonstrated $hk1$ dominated growth *via* the solution-processed spin coating method.[18] Fig. 4(g) shows that 2.5-Sb_2S_3 obtained the highest texture coefficient (2.62 ($hk1/hk0$)) among all the samples, clearly indicating its superior $hk1$ growth characteristic. The pronounced $hk1$-oriented growth observed in the 2.5-Sb_2S_3 sample can be linked to an optimal balance between sulphur availability and nucleation kinetics. Tuning the CS_2 concentration in the precursor solution to 2.5 ml resulted in a sufficient supply of sulphur to saturate nucleation sites and promote crystal growth in the desired $hk1$ orientation. Increasing the concentration of CS_2 further to 3.0 ml drives the system to enter a state of supersaturation, which leads to rapid, uncontrolled nucleation. This results in the formation of smaller nanocrystals (proven by the dense diffraction spots and bright-field TEM images) instead of continued growth of existing crystals, producing non-uniform orientations and a reduction of $hk1$-oriented growth. However, both 2.5-Sb_2S_3 (c) and 3.0-Sb_2S_3 (d) show favourable $hk1$ oriented film growth (2.62 and 1.86, respectively) compared to 1.5-Sb_2S_3 (a) and 2.0-Sb_2S_3 (b) (1.23 and 0.70, respectively). The lower TC values obtained for 1.5-Sb_2S_3 and 2.0-Sb_2S_3 could be attributed to the unavailability of sulphur, for promoting $hk1$ growth. The Miller indices (101), (111), (211), (221), (311), and (411) match well with other research papers.[20,31,32,36–38] Hence, the TC measurements show that the 2.5-Sb_2S_3 $(Sb_4S_6)_n$ ribbons achieved the overall highest texture coefficients ($TC_{(hk1)}/TC_{(hk0)}$). Images in Fig. 4(e) and (f) were captured with an external camera to display the SAED pattern rings visible to the naked eye to confirm the crystallinity as these specific images were unable to be captured with the TEM camera due to its chances of getting burnt. Therefore, the TCs measured from the SAED pattern of the fabricated films revealed that tuning of the precursor's concentration can generate Sb_2S_3 films with $hk1$-oriented crystal growth.

3.4. Energy dispersive X-ray spectroscopy (EDS)

An energy dispersive X-ray spectrometer equipped with a scanning electron microscope was employed to determine the elemental composition and distribution of the synthesized Sb_2S_3 samples and to verify their chemical stoichiometry. An accelerating voltage of 20.00 kV, working distance of 10.5 mm, (×30) magnification and high vacuum mode were utilized to perform EDS. The atomic percentage was evaluated by composition analysis, and the elemental distribution was found by performing area mapping. Fig. 5(a)–(d) show that all 4 samples (1.5-Sb_2S_3, 2.0-Sb_2S_3, 2.5-Sb_2S_3, and 3.0-Sb_2S_3, respectively) reached the ideal stoichiometric ratio of 2 : 3 (Sb : S).[19,39] The change in concentration of the CS_2 in the precursor solution did not seem to affect the end stoichiometric ratio much, whereas in other techniques, careful adjustments to the deposition factors need to be made to reach the ideal stoichiometric ratio.[38,40] This elemental composition analysis ensures that 2.5-Sb_2S_3 and 3.0-Sb_2S_3, Fig. 5(c) and (d), respectively, possess optimal composition (ideal stoichiometric ratio), along with superior morphological, structural, and $hk1$-oriented growth properties, as revealed by BF-TEM and SAED patterns. Fig. 5(e)–(h) show the elemental distribution of 1.5-Sb_2S_3, 2.0-Sb_2S_3, 2.5-Sb_2S_3 and 3.0-Sb_2S_3, respectively. It is worth noting that a layer of platinum was deposited onto the Sb_2S_3 film before this measurement. These distribution mapping images confirm the uniform spread of Sb_2S_3 throughout the substrate. However, images in Fig. 5(g) and (h) show some flaws regarding the distribution of Sb and S. To its justification, the area uncovered by Sb and S in the image of Fig. 5(g) is due to that location being covered by an adhesive tape, which prevented the deposition of the solution. Other areas in the sample possessed a uniform distribution. The image in Fig. 5(h) shows a rather unequal distribution of Sb and S along the surface. This could be because this image corresponds to an edge of the sample; however, there were other locations present with more uniform spread out (data not shown). Furthermore, 2.5-Sb_2S_3 (Fig. 5(g)) seemed to possess the least amount of carbon residue. 3.0-Sb_2S_3 (Fig. 5(h)) was observed to have some carbon residue left from the precursor solution but less than 1.5-Sb_2S_3 and 2.0-Sb_2S_3 (data not shown). Regarding this, further rigorous annealing may generate carbon-free films across all the samples; however, this may lead to the development of undesirable grain boundaries at the micron scale. As all the samples were deposited and annealed under the same conditions (spin-coated at 6000 rpm for 30 seconds and annealed at 300 °C), it can be concluded that adding 2.5 ml of CS_2 can generate an almost carbon-free, uniformly distributed Sb_2S_3 film.

3.5. Variable angle spectroscopic ellipsometry

Variable Angle Spectroscopic Ellipsometry (VASE) was employed for the measurement of optical properties (absorption coefficient and bandgap) and constants (n and k) using the same fitting model. Fig. 6(a) shows the absorption coefficient spectrum across the wavelength range 300–1600 nm. The 2.5 ml CS_2 used sample (2.5-Sb_2S_3), in red colour, displays the overall greatest absorption across the measured wavelengths. While the final stoichiometric ratio remains almost similar for all four samples, variation in CS_2 significantly impacts the intermediate stages of film formation. The increased 2.5 ml CS_2 concentration likely favours modulating precursor solubility, controlling nucleation kinetics and directing crystal growth planes. The superior light absorption for 2.5-Sb_2S_3 could therefore be attributed to its larger crystals and preferable $hk1$-oriented growth. The improved morphological uniformity of 2.5-Sb_2S_3

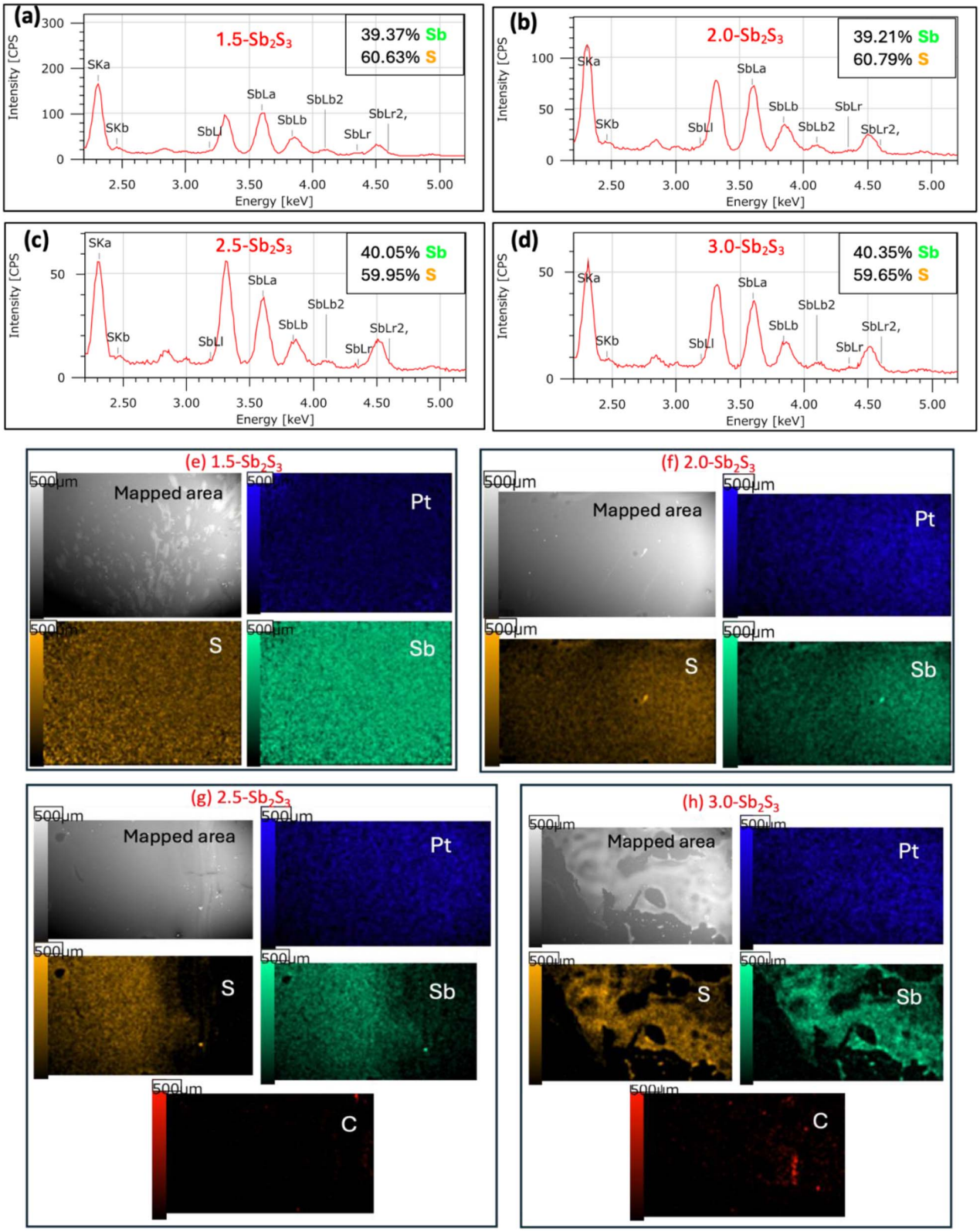

Fig. 5 Energy dispersive X-ray spectroscopy (EDS) compositional analysis of (a) 1.5-Sb_2S_3, (b) 2.0-Sb_2S_3, (c) 2.5-Sb_2S_3 and (d) 3.0-Sb_2S_3. Elemental distribution analysis of (e) 1.5-Sb_2S_3, (f) 2.0-Sb_2S_3, (g) 2.5-Sb_2S_3 and (h) 3.0-Sb_2S_3.

contributes further to reducing reflection losses, improving absorption. 2.0-Sb_2S_3 exhibits spectral fluctuations, which may be attributed to thickness inhomogeneities and surface roughness. Overall, these results show the potential optimization of absorption properties through strategic tuning of the precursor concentration.

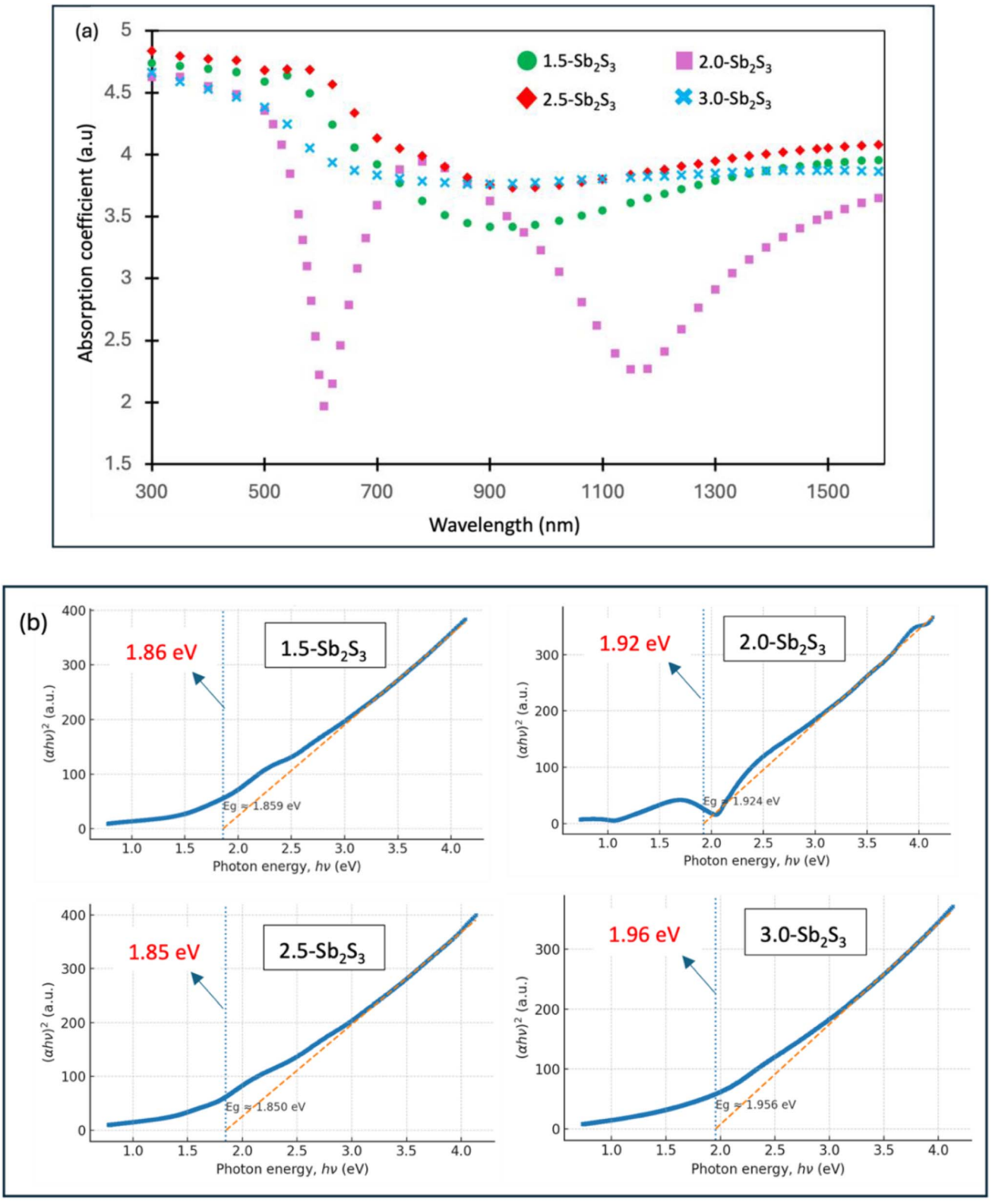

Fig. 6 Variable angle spectroscopic ellipsometry (VASE) analysis of (a) absorption coefficient spectrum of 1.5-Sb_2S_3, 2.0-Sb_2S_3, 2.5-Sb_2S_3, and 3.0-Sb_2S_3. (b) Tauc plots of 1.5-Sb_2S_3, 2.0-Sb_2S_3, 2.5-Sb_2S_3, and 3.0-Sb_2S_3 showing the direct optical bandgap.

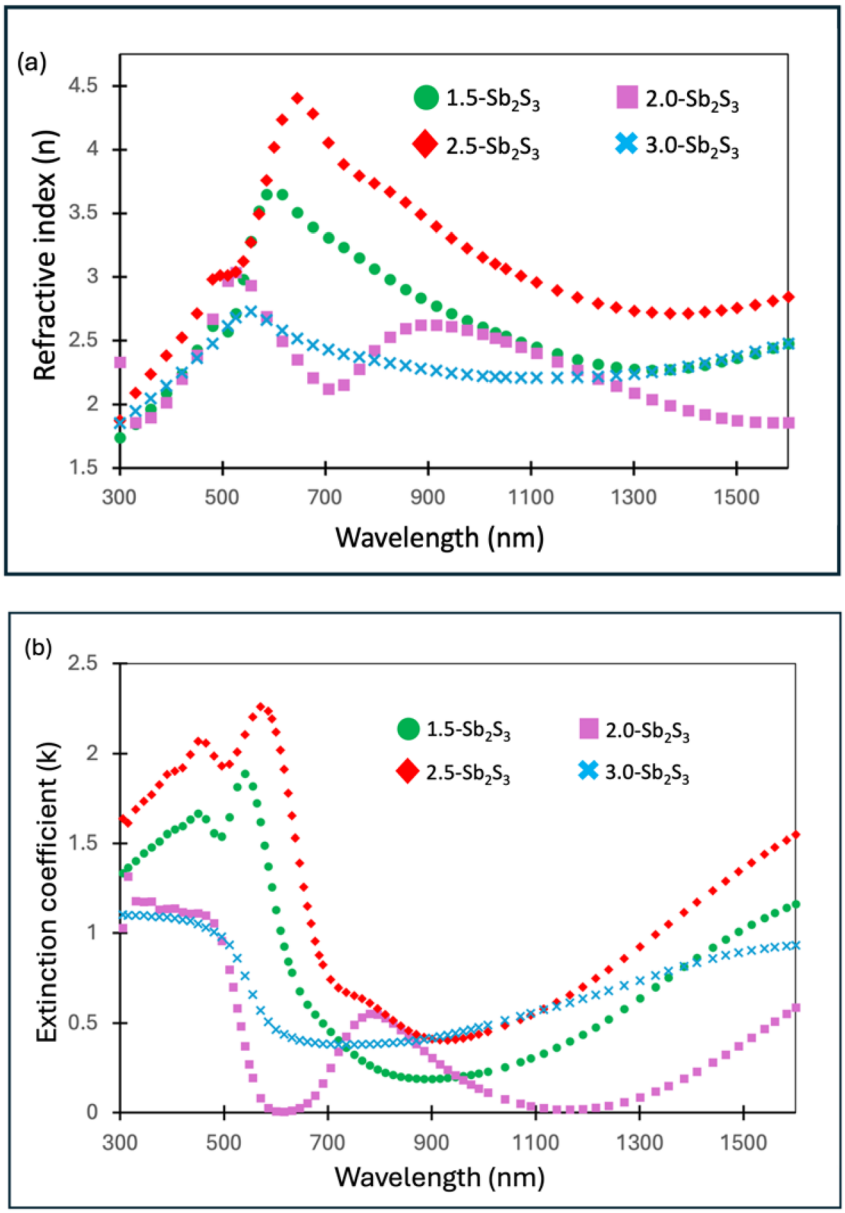

Fig. 7 Variable angle spectroscopic ellipsometry (VASE) analysis of (a) the refractive index (n) spectrum of 1.5-Sb_2S_3, 2.0-Sb_2S_3, 2.5-Sb_2S_3, and 3.0-Sb_2S_3; (b) extinction coefficients (k) of 1.5-Sb_2S_3, 2.0-Sb_2S_3, 2.5-Sb_2S_3, and 3.0-Sb_2S_3.

The optical bandgaps of the films were evaluated using the equation given below (eqn 2):

$$(\alpha h\nu)^n = A(h\nu - E_g) \quad (2)$$

where E_g is the optical bandgap, α is the absorption coefficient, ν is the frequency, h is the Planck constant, A is a material constant, and $n = 2$, 1/2, and 2/3, respectively, for allowed direct, allowed indirect, and forbidden direct transitions.

Allowed direct transition ($n = 2$) was used to obtain the bandgap values as they generated a smooth linear fit to the graph, and the corresponding Tauc plots are shown in Fig. 6(b). This confirms that all the fabricated Sb_2S_3 thin films are direct bandgap semiconductor materials, as has been reported before.[41] From direct Tauc plot extrapolations, the optical bandgaps of the Sb_2S_3 thin films fall within a narrow range of 1.85–1.96 eV: 1.5-Sb_2S_3 – 1.86 eV, 2.0-Sb_2S_3 – 1.92 eV, 2.5-Sb_2S_3 – 1.85 eV, and 3.0-Sb_2S_3 – 1.96 eV. Rajpure and Bhosale[42] reported a direct bandgap of 1.88 eV with a stoichiometric composition of 2 : 3 (Sb : S) which is very similar to our obtained values, also using a solution-processed approach. The range of values obtained in this research work also aligns well with other reports of Sb_2S_3 thin film.[20,36] Slight changes in E_g values could be due to the combined effect of microstructural variations in crystal size, structural disorder, and thickness inhomogeneity. The minimal variations in E_g indicate that CS_2 concentration has more influence on the film's crystal size and growth direction than on altering the intrinsic electronic structure. To further justify the

narrow range of bandgap values, as all the samples were heated at the same temperature (300 °C), environment (vacuum) and duration (30 minutes), the films possessed similar bandgaps. Larger changes in bandgaps are often observed with changes in the annealing temperature or the end stoichiometric ratio, which in our case are almost constant across all the samples (1.5-Sb_2S_3, 2.0-Sb_2S_3, 2.5-Sb_2S_3, and 3.0-Sb_2S_3).[19,42] Large changes in E_g can be obtained by varying electrodeposited potentials, with Al_2Te_3 having the E_g range of (2.26–2.68 eV), much higher than the reported values of Sb_2S_3 (1.85–1.96 eV) here.[43]

In recent research advances, it has become increasingly important to optimize optical constants (refractive index and extinction coefficient) for the innovation of new opto-electronic devices.[44] Enhancing the refractive index of Sb_2S_3 receives great importance due to its potential application in high-reflecting dielectric films.[19] Fig. 7(a) and (b) show the refractive index (n) and extinction coefficient (k) of the Sb_2S_3 film, respectively. 2.5-Sb_2S_3 (2.5 ml CS_2) was observed to achieve the highest overall refractive index among the four samples over the wide wavelength range from 300 nm to 1600 nm. The obtained high n value of 2.5-Sb_2S_3 could be correlated to larger nanocrystals, as shown previously in bright-field TEM, combined with film compactness. The enhanced refractive index value obtained in this research work due to the strategic tuning of the precursor concentration is found to be higher than other reported values of Sb_2S_3.[16,19,45–47] Moreover, some reported research studies show similar refractive index values as obtained here, but they utilized a more expensive non-solution based approach.[44,48,49] Hence, it could be concluded that the proposed strategic tuning of the precursor concentration can result in a much higher refractive index (n) value than the usual. The extinction coefficient (k) quantifies how effectively a material absorbs light at a specific wavelength and is linked to the absorption coefficient (α) (eqn (3)).[50] A greater absorption coefficient would generate a greater extinction coefficient (k) value.

$$\alpha = \frac{4\pi k}{\lambda} \tag{3}$$

Our obtained experimental results of 2.5-Sb_2S_3 agree with this statement, achieving the overall highest α and k among all the samples. Fig. 7(b) shows the extinction coefficient (k) spectrum over the wavelength ranging from 300 to 1600 nm. As can be clearly observed from the plots of the curves, 2.5-Sb_2S_3 possesses the highest overall extinction coefficient (k) values. Such properties are excellent for applications that require efficient light harvesting in thin layers (~100 nm), such as photovoltaics and photodetectors. The superior k value achieved by 2.5-Sb_2S_3 could correlate with a denser packed film with improved surface morphology and preferred orientation ($hk1$) of the crystal planes coupled together. The reported k value of 2.5-Sb_2S_3 in this research work is higher compared to other reported values of Sb_2S_3 films.[46,49] Extinction coefficient (k) values reported by Medina-Montes *et al.*[48] are similar to the k values that we have achieved for 2.5-Sb_2S_3 over the visible to near-infrared spectrum. Hence, this concludes that strategic tuning of the precursor concentration can effectively enhance the extinction coefficient (k) values.

4. Conclusion

Comprehensive structural, compositional, and optical investigations confirm the successful synthesis of Sb_2S_3 thin films with tuneable properties through controlled variation of the CS_2 precursor concentration. Bright-field TEM images revealed that 2.5-Sb_2S_3 (precursor solution synthesized with 2.5 ml CS_2) obtained the largest nanocrystals (~120 nm). High-resolution TEM images along with FFT-diffractogram images revealed the pure crystalline phase with clear lattice fringes and without any evident defects. SEM images of all the samples confirmed the overall compact, homogeneous surface morphology with the absence of any dense grain boundary location across all the fabricated films, at the micron scale. SAED ring patterns revealed the presence of dense diffraction spot regions, which indicated the existence of smaller crystals. The Miller indices, calculated from the d-spacing of the SAED rings, helped identify the crystal planes. The texture coefficient ($hk1/hk0$) measurements revealed the superior $hk1$-oriented growth of 2.5-Sb_2S_3, obtaining the highest $hk1/hk0$ texture coefficient of 2.62. EDS measurements revealed the presence of the ideal stoichiometric ratio (Sb : S, 2 : 3) across all the samples, with 2.5-Sb_2S_3 being almost carbon-free. These structural, compositional observations directly correlated with the optical behaviour extracted from VASE measurements, where all samples exhibited direct band gaps in the range of 1.85–1.96 eV, in agreement with reported values for Sb_2S_3. Importantly, a clear distinction emerged among the samples: the 2.5 ml CS_2 composition consistently showed superior optical performance, with the highest absorption coefficient, enhanced refractive index (n), and extinction coefficient (k), indicating efficient light–matter interaction. In contrast, films prepared with either lower or higher CS_2 concentrations exhibited weaker optical responses, suggesting that precursor chemistry plays a decisive role in balancing nucleation and growth kinetics. Taken together, these results identify the 2.5 ml CS_2-derived Sb_2S_3 thin film as the optimum recipe, combining enlarged crystal size and favourable $hk1$-oriented growth, to obtain superior optical response and highlight its strong potential for integration into next-generation photovoltaic and optoelectronic devices.

Author contributions

Md Abrar Faisal Hossain: conceptualization, formal analysis, investigation, methodology, visualization, writing – original draft, writing – review & editing. Kyota Shirai: investigation, methodology, project administration, resources. Masayuki Shimojo: funding acquisition, supervision, writing – review & editing.

Conflicts of interest

The authors confirm that there are no conflict of interests.

Data availability

The authors confirm that the data supporting the findings of this research work can be found in this article. ImageJ software was used for analysing TEM images and indexing SAED patterns. Microsoft Excel was used for plotting the graphs. Microsoft Word was used for writing the research article.

Acknowledgements

The authors acknowledge Prof. Masayuki Shimojo's research group for support with TEM, SEM, and VASE measurements. The authors also acknowledge the support of Prof. Shu Ping Lau (https://orcid.org/0000-0002-5315-8472), which helped with conceptualization of the research work. The authors have no funding source to declare.

References

1 Z. Li and Y. Tian, Nano-Bismuth-Sulfide for Advanced Optoelectronics, *Photonics*, 2022, **9**, 790, DOI: 10.3390/photonics9110790.

2 Z. Cai, J. Sun, H. Cai, Y. Gu, R. Tang, C. Zhu, P. Luo and T. Chen, Sb_2Se_3 as a bottom cell material for efficient perovskite/Sb_2Se_3 tandem solar cells, *Energy Mater. Devices*, 2024, **2**, 9370027, DOI: 10.26599/EMD.2024.9370027.

3 R. Tang, X. Wang, C. Jiang, S. Li, W. Liu, H. Ju, S. Yang, C. Zhu and T. Chen, n-Type doping of Sb_2S_3 light-harvesting films enabling high-efficiency planar heterojunction solar cells, *ACS Appl. Mater. Interfaces*, 2018, **10**, 30314–30321, DOI: 10.1021/acsami.8b08965.

4 P. Kumar, M. Eriksson, D. S. Kharytonau, S. You, M. M. Natile and A. Vomiero, All-Inorganic Hydrothermally Processed Semitransparent Sb_2S_3 Solar Cells with CuSCN as the Hole Transport Layer, *ACS Appl. Energy Mater.*, 2024, **7**(4), 1421–1432, DOI: 10.1021/acsaem.3c02492.

5 T. Shi, J. Zheng, X. Wang, P. Zhang, P. Zong and K. M. Razeeb, Recent advances of electrodeposition of Bi_2Te_3 and its thermoelectric applications in miniaturized power generation and cooling, *Int. Mater. Rev.*, 2023, **68**(5), 521–555, DOI: 10.1080/09506608.2022.2145359.

6 H. Mamur, O. F. Dilmac, H. Korucu and M. R. A. Bhuiyan, Cost-effective chemical solution synthesis of bismuth telluride nanostructure for thermoelectric applications, *Micro Nano Lett.*, 2018, **13**(8), 1117–1120, DOI: 10.1049/mnl.2018.0116.

7 C. Krataithong, K. Srichai, E. Wongrat and A. Tubtimtae, Comparative study on the influence of transparent glass substrates for antimony telluride thin films via structural and optical properties, *J. Sci.: Adv. Mater. Devices*, 2022, **7**(3), 100449, DOI: 10.1016/j.jsamd.2022.100449.

8 A. Lawal, A. Shaari, R. Ahmed and N. Jarkoni, Sb_2Te_3 crystal a potential absorber material for broadband photodetector: A first-principles study, *Results Phys.*, 2017, **7**, 2302–2310, DOI: 10.1016/j.rinp.2017.06.040.

9 P. Priyadarshini, S. Das and R. Naik, A review on metal-doped chalcogenide films and their effect on various optoelectronic properties for different applications, *RSC Adv.*, 2022, **12**(16), 9599–9620, DOI: 10.1039/D2RA00771A.

10 Z. Fan, K. Yan, L. Zhang, J. Qin, J. Chen, R. Wang and X. Shen, Design and fabrication of As_2Se_3 chalcogenide waveguides with low optical losses, *Appl. Opt.*, 2020, **59**(6), 1564–1570, DOI: 10.1364/AO.386280.

11 P. Chaiworn, P. Nantawiang, E. Wongrat, P. Nedkun, P. Pramukkul and A. Tubtimtae, Effect of antimony oxide incorporation on the structural, optical, and electrical properties of multiphase bismuth telluride thin films, *Opt. Mater.*, 2025, **168**, 117514, DOI: 10.1016/j.optmat.2025.117514.

12 S. S. Harke, T. Zhang, R. Huang and C. Gurnani, Solution-based in situ deposition of Sb2S3 from a single source precursor for resistive random-access memory devices, *Mater. Adv.*, 2023, **4**(18), 4119–4128, DOI: 10.1039/D3MA00205E.

13 M. Zhang, R. Wang, X. Zou, S. Song, Y. Bao, L. Wu, Z. Song and X. Zhou, Understanding the microstructure evolution of carbon-doped Sb_2Te_3 phase change material for high thermal stability memory application, *Appl. Phys. Lett.*, 2024, **124**(20), 202101, DOI: 10.1063/5.0206244.

14 S. Liu, W. Liu, W. Lyu, H. Gao, D. V. Golberg and Z. Chen, Defect engineering in van der Waals layer-structured Bi_2Te_3-based materials, *cMat*, 2025, **2**(2), e70009, DOI: 10.1002/cmt2.70009.

15 D. Vega, R. Picos, A. Rodriguez, Y. Gupta, O. Camps, E. Saucedo, J. Puigdollers, C. de Benito, J. Llorca and S. G. Stavrinides, A circuital model of Sb_2Se_3 solar cells as memdiode devices for neuromorphic applications, *IEEE Trans. Electron Devices*, 2025, **72**(4), 2078–2085, DOI: 10.1109/TED.2025.3546192.

16 H. Maghraoui-Meherzi, T. Ben Nasr, N. Kamoun and M. Dachraoui, Physical properties of chemically deposited Sb_2S_3 thin films, *C. R. Chim.*, 2011, **14**(5), 471–475, DOI: 10.1016/j.crci.2010.10.007.

17 C. D. Lokhande, B. R. Sankapal, R. S. Mane, H. M. Pathan, M. Muller, M. Giersig and V. Ganesan, XRD, SEM, AFM, HRTEM, EDAX and RBS studies of chemically deposited Sb_2S_3 and Sb_2Se_3 thin films, *Appl. Surf. Sci.*, 2002, **193**(1–4), 1–10, DOI: 10.1016/S0169-4332(01)00819-4.

18 Z. Chen, X. Chen, J. Zhou, B. Tang, Y. Li, X. Yang and R. Zhou, Evaluating the film orientation and grain boundary of vacuum- and solution-processed Sb_2S_3 films toward efficient solar cells, *Energy Fuels*, 2024, **38**(22), 22536–22542, DOI: 10.1021/acs.energyfuels.4c04739.

19 F. Perales, G. Lifante, F. Agulló-Rueda and C. de las Heras, Optical and structural properties in the amorphous to polycrystalline transition in Sb_2S_3 thin films, *J. Phys. D: Appl. Phys.*, 2007, **40**(8), 2440–2444, DOI: 10.1088/0022-3727/40/8/005.

20 V. Vinayakumar, C. R. O. Hernández, S. Shaji, D. A. Avellaneda, J. A. A. Martinez and B. Krishnan, Effects of rapid thermal processing on chemically deposited antimony sulfide thin films, *Mater. Sci. Semicond. Process.*, 2018, **80**, 9–17, DOI: 10.1016/j.mssp.2018.02.011.

21 S. Yuan, H. Deng, D. Dong, X. Yang, K. Qiao, C. Hu, H. Song, H. Song, Z. He and J. Tang, Efficient planar antimony sulfide thin film photovoltaics with large grain and preferential growth, *Sol. Energy Mater. Sol. Cells*, 2016, **157**, 887–893, DOI: 10.1016/j.solmat.2016.07.050.

22 X. Wang, J. Li, W. Liu, S. Yang, C. Zhu and T. Chen, A fast chemical approach towards Sb_2S_3 film with a large grain size for high-performance planar heterojunction solar cells, *Nanoscale*, 2017, **9**(10), 3386–3390, DOI: 10.1039/C7NR00154A.

23 Y. C. Choi, D. U. Lee, J. H. Noh, E. K. Kim and S. I. Seok, Highly improved Sb_2S_3 sensitized-inorganic-organic heterojunction solar cells and quantification of traps by deep-level transient spectroscopy, *Adv. Funct. Mater.*, 2014, **24**(23), 3587–3592, DOI: 10.1002/ADFM.201304238.

24 R. K. Sahoo, S. Singh, J. M. Yun, S. H. Kwon and K. H. Kim, Sb_2S_3 nanoparticles anchored or encapsulated by the sulphur-doped carbon sheet for high-performance supercapacitors, *ACS Appl. Mater. Interfaces*, 2019, **11**(37), 33966–33977, DOI: 10.1021/ACSAMI.9B11028.

25 J. Luo, W. Xiong, G. Liang, Y. Liu, H. Yang, Z. Zheng, X. Zhang, P. Fan and S. Chen, Fabrication of Sb_2S_3 thin films by magnetron sputtering and post-sulfurization/selenization for substrate structured solar cells, *J. Alloys Compd.*, 2020, **826**, 154235, DOI: 10.1016/J.JALLCOM.2020.154235.

26 R. Fukuda, T. Nishimura and A. Yamada, Experimental and theoretical EBIC analysis for grain boundary and CdS/Cu(In,Ga)Se_2 heterointerface in Cu(In,Ga)Se_2 solar cells, *Prog. Photovoltaics Res. Appl.*, 2023, **31**(7), 678–689, DOI: 10.1002/PIP.3673.

27 Y. C. Choi and S. I. Seok, Efficient Sb_2S_3-sensitized solar cells via single-step deposition of Sb_2S_3 using S/Sb-ratio-controlled $SbCl_3$-thiourea complex solution, *Adv. Funct. Mater.*, 2015, **25**(19), 2892–2898, DOI: 10.1002/ADFM.201500296.

28 W. Wang, P. Pfeiffer and L. Schmidt-Mende, Direct patterning of metal chalcogenide semiconductor materials, *Adv. Funct. Mater.*, 2020, **30**(27), 2002685, DOI: 10.1002/ADFM.202002685.

29 Y. Yin, C. Wu, R. Tang, C. Jiang, G. Jiang, W. Liu, T. Chen and C. Zhu, Composition engineering of Sb_2S_3 film enabling high performance solar cells, *Sci. Bull.*, 2019, **64**(2), 136–141, DOI: 10.1016/J.SCIB.2018.12.013.

30 A. Maiti, S. Chatterjee and A. J. Pal, Sulfur-vacancy passivation in solution-processed Sb_2S_3 thin films: influence on photovoltaic interfaces, *ACS Appl. Energy Mater.*, 2020, **3**(1), 810–821, DOI: 10.1021/ACSAEM.9B01951.

31 S. Wang, Y. Zhao, B. Che, C. Li, X. Chen, R. Tang, J. Gong, X. Wang, G. Chen, T. Chen, J. Li and X. Xiao, A novel multi-sulphur source collaborative chemical bath deposition technology enables 8%-efficiency Sb_2S_3 planar solar cells, *Adv. Mater.*, 2022, **34**(41), 2206242, DOI: 10.1002/ADMA.202206242.

32 W. Qiu, R. Lei, X. Tang, Y. Tang, X. Huang, K. Zhang, Z. Lin, S. Xiao, X. Wang and S. Yang, Sulfur-supplemented vapor transport deposition of Sb_2S_3 and $Sb_2(S,Se)_3$ for high-performance hydrogen evolution photocathodes, *Sol. RRL*, 2024, **8**(5), 2300876, DOI: 10.1002/SOLR.202300876.

33 X. Jin, Y. Fang, T. Salim, M. Feng, S. Hadke, S. W. Leow, T. C. Sum and L. H. Wong, In situ growth of [hk1]-oriented Sb_2S_3 for solution-processed planar heterojunction solar cell with 6.4% efficiency, *Adv. Funct. Mater.*, 2020, **30**(35), 2002887, DOI: 10.1002/ADFM.202002887.

34 Y. Huang, R. Tang, P. Xiao, B. Che, Y. Wang, H. Gao, G. Wang, C. Zhu and T. Chen, Efficient in situ sulfuration process in hydrothermally deposited Sb_2S_3 absorber layers, *ACS Appl. Mater. Interfaces*, 2022, **14**(49), 54822–54829, DOI: 10.1021/ACSAMI.2C17912.

35 J. Han, S. Wang, J. Yang, S. Guo, Q. Cao, H. Tang, X. Pu, B. Gao and X. Li, Solution-processed Sb_2S_3 planar thin film solar cells with a conversion efficiency of 6.9% at an open circuit voltage of 0.7 V achieved via surface passivation by a $SbCl_3$ interface layer, *ACS Appl. Mater. Interfaces*, 2020, **12**(4), 4970–4979, DOI: 10.1021/ACSAMI.9B15148.

36 X. Duan, A. Amin, Y. Wang and F. Yan, Grain engineering of solution-processed Sb_2S_3 thin film by tuning precursor fabrication environments, *Results Surf. Interfaces*, 2024, **16**, 100251, DOI: 10.1016/J.RSURFI.2024.100251.

37 D. C. Onwudiwe, O. C. Olatunde and S. Mathur, Structural studies and morphological properties of antimony sulphide nanorods obtained by solvothermal synthesis, *Phys. B Condens. Matter*, 2021, **605**, 412691, DOI: 10.1016/J.PHYSB.2020.412691.

38 B. Krishnan, A. Arato, E. Cardenas, T. K. D. Roy and G. A. Castillo, On the structure, morphology, and optical properties of chemical bath deposited Sb_2S_3 thin films, *Appl. Surf. Sci.*, 2008, **254**(10), 3200–3206, DOI: 10.1016/J.APSUSC.2007.10.098.

39 F. Cao, W. Liu, L. Zhou, R. Deng, S. Song, S. Wang, S. Su and H. Zhang, Well-defined Sb_2S_3 microspheres: High-yield synthesis, characterization, their optical and electrochemical hydrogen storage properties, *Solid State Sci.*, 2011, **13**(6), 1226–1231, DOI: 10.1016/J.SOLIDSTATESCIENCES.2011.02.007.

40 D. M. Kavya, B. J. Prabhu, N. J. Choudhari, M. J. Panjikaran, S. D. George, S. D. Kulkarni, V. Mishra and Y. Raviprakash, Two-step synthesis of antimony sulfide thin films: enhancement in physical properties through sulfurization, *Mater. Res. Express*, 2024, **11**(4), 046402, DOI: 10.1088/2053-1591/AD3897.

41 S. Messina, M. T. S. Nair and P. K. Nair, Solar cells with Sb_2S_3 absorber films, *Thin Solid Films*, 2009, **517**(7), 2503–2507, DOI: 10.1016/j.tsf.2008.11.060.

42 K. Y. Rajpure and C. H. Bhosale, Effect of composition on the structural, optical and electrical properties of sprayed Sb_2S_3 thin films prepared from non-aqueous medium, *J. Phys. Chem. Solids*, 2000, **61**(4), 561–568, DOI: 10.1016/S0022-3697(99)00240-1.

43 N. Suwannakham and A. Tubtimtae, Synthesis of aluminum telluride thin films via using electrodeposition method for solar absorber applications, *Mater. Lett.*, 2023, **336**, 133920, DOI: 10.1016/j.matlet.2023.133920.

44 T. Ben Nasr, H. Maghraoui-Meherzi, H. Ben Abdallah and R. Bennaceur, Electronic structure and optical properties of Sb_2S_3 crystal, *Phys. B Condens. Matter*, 2011, **406**(2), 287–292, DOI: 10.1016/j.physb.2010.10.070.

45 A. M. Salem and M. S. Selim, Structure and optical properties of chemically deposited Sb_2S_3 thin films, *J. Phys. D: Appl. Phys.*, 2001, **34**(1), 12–17, DOI: 10.1088/0022-3727/34/1/303.

46 F. Aousgi, W. Dimassi, B. Bessais and M. Kanzari, Effect of substrate temperature on the structural, morphological, and optical properties of Sb_2S_3 thin films, *Appl. Surf. Sci.*, 2015, **350**, 19–24, DOI: 10.1016/j.apsusc.2015.01.126.

47 N. Tigau, Influence of thermoannealing on crystallinity and optical properties of Sb_2S_3 thin films, *Cryst. Res. Technol.*, 2007, **42**(3), 281–285, DOI: 10.1002/crat.200610813.

48 M. I. Medina-Montes, Z. Montiel-González, F. Paraguay-Delgado, N. R. Mathews and X. Mathew, Structural, morphological and spectroscopic ellipsometry studies on sputter deposited Sb_2S_3 thin films, *J. Mater. Sci.: Mater. Electron.*, 2016, **27**(9), 9710–9719, DOI: 10.1007/s10854-016-5033-0.

49 E. Gnenna, N. Khemiri, M. I. Alonso and M. Kanzari, Optical characterization of Sb_2S_3 vacuum annealed films by UV–VIS–NIR spectroscopy and spectroscopic ellipsometry: Determining the refractive index and the optical constants, *Optik*, 2022, **268**, 169740, DOI: 10.1016/j.ijleo.2022.169740.

50 P. Priyadarshini, S. Das, D. Alagarasan, R. Ganesan, S. Varadharajaperumal and R. Naik, Role of Bismuth incorporation on the structural and optical properties in BixIn35-xSe65 thin films for photonic applications, *J. Am. Ceram. Soc.*, 2021, **104**(11), 5803–5814, DOI: 10.1111/jace.17960.